2006

Modeling of Transport Phenomena and Melting Kinetics of Starch in a Co-Rotating Twin-Screw Extruder

Lijun Wang
North Carolina Agricultural & Technical State University, lwang@ncat.edu

David D. Jones
University of Nebraska-Lincoln, david.jones@unl.edu

Curtis L. Weller
University of Nebraska-Lincoln, cweller1@unl.edu

Milford Hanna
University of Nebraska-Lincoln, mhanna1@unl.edu

Published in *Advances in Polymer Technology* 25:1 (2006), pp. 22–40;
doi: 10.1002/adv.20055

A contribution of the University of Nebraska Agricultural Research Division, Lincoln, NE, Journal Series No. 14515.
Contract grant sponsor: U.S. Department of Energy and the Hatch Act.

Submitted February 18, 2005; revised: October 17, 2005.

Modeling of Transport Phenomena and Melting Kinetics of Starch in a Co-Rotating Twin-Screw Extruder

Lijun Wang, David D. Jones, Curtis L. Weller, and Milford A. Hanna

Industrial Agricultural Products Center, Department of Biological Systems Engineering, University of Nebraska-Lincoln, Lincoln, NE 68583-0726

Corresponding author — Lijun Wang; email lwang5@unl.edu

Abstract
A mathematical model was developed to simulate fluid flow, heat transfer, and melting kinetics of starch in a co-rotating intermeshing twin-screw extruder (TSE). The partial differential equations governing the transport phenomena of the biomaterial in the extruder were solved by a finite element scheme. For validating the model, the predicted product pressure, bulk temperature at the entrance of the die, and minimum residence time of the biomaterial in the extruder were compared with experimental data. Standard errors of product pressure, bulk temperature at the die entrance, and minimum residence time were about 8.8, 2.8, and 17.3%. Simulations were carried out to investigate profiles of product pressure, bulk temperature, and melt fraction within the extruder during extrusion.

Keywords: biomaterials, computer modeling, extrusion, numerical analysis, starch, transport

Introduction

Twin-screw extruders are used widely in the manufacture of food and feed products, pharmaceuticals, and plastics because of their advantages such as excellent feeding and mixing capacities, as compared with a single-screw extruder. Twin-screw extruders consist of two screws, having a "figure-eight" cross section, mounted in a barrel. There are a large number of types of twin-screw extruders. The co-rotating intermeshing twin-screw extruder is one of the most frequently used designs.[1] The main difference between the screw channels of a co-rotating intermeshing twin-screw extruder and a single-screw extruder is the existence of an intermeshing region in the twin-screw channel. Therefore, the twin-screw channel has two regions: the C-shaped region and the intermeshing region.[1–3]

The existence of the intermeshing region in the twin-screw channel results in a special fluid flow region in the channel. In the co-rotating intermeshing twin-screw extruder, the flow from one screw channel is divided into two streams: one part remains in the same screw channel and goes through the intermeshing region, and the other part goes into the other screw channel. In the intermeshing region, the flow from one screw channel interacts with the flow from the other screw channel. The interaction of two flow streams increases the mixing and heat transfer capacities of the extruder.[4] The conveying section of a co-rotating twin screw is always partially filled.[1] Barres et al.[5] reported degrees of filling, in the conveying section, in the range of 1–40%. Modeling of transport phenomena and melting kinetics in a twin-screw extruder has been carried out in the past two decades. A literature review showed that most of the models focused on just one of the complex phenomena such as heat transfer, melting kinetics, or fluid flow, which occur in a twin-screw extruder. Sastrohartono et al.[6] analyzed numerically the fluid flow and heat transfer in the melt pumping section of twin-screw extruders. They divided the complex geometry of the twin-screw extruder into repeated "C" regions and intermeshing regions. Tayeb et al.[3] developed a model to predict the pressure generation in a C-shaped chamber and pressure drop in an intermeshing chamber. Usually, the heat was assumed to be transferred from the hot barrel wall to the material bed by convection in a twin-screw extruder and a pseudo-convection heat transfer coefficient was used.[1,3,7,8] Rauwendaal[9] observed that the dispersed solids melting (DSM) phenomenon occurred in a twin-screw extruder. During DSM, the solid particles were dispersed uniformly in a melt matrix and melted gradually. Zhu et al.[10] developed a model to describe the DSM in co-rotating twin-screw extrusion.

However, no publications were found on the simultaneous analysis of fluid flow, heat transfer, and melting kinetics in a co-rotating twin-screw extruder. In this paper, such a mathematical model is developed. The model was validated by experiments. The model was further used to predict the profiles of the product pressure, bulk temperature, and melting fraction during extrusion.

Mathematical Model

The model was divided into four parts: (1) geometrical description to determine the parameters of the channel for fluid flow and heat transfer, (2) fluid flow to predict the flow patterns and pressure gradients in the extruder, (3) melting kinetics and heat transfer to determine the melting rate and the temperature profiles of product along the extruder, and (4) mixing in the extruder.

Geometrical Description

A typical co-rotating intermeshing twin-screw extruder is shown in Figure 1a. The central part of the extruder has two screws. The twin-screw channel has two repeated regions: the C-shaped region and the intermeshing region as shown in Figure 1b. In order to simplify the analysis, the real extruder was depicted schematically as a sequence of C-shaped chambers and intermeshing chambers as shown in Figure 1c.

The following assumptions were made for describing the geometry of the channel:

(1) The channel in the C-shaped region was assumed to have a rectangular cross-section, with average height H_{cn} and width B_{cn}.[2]

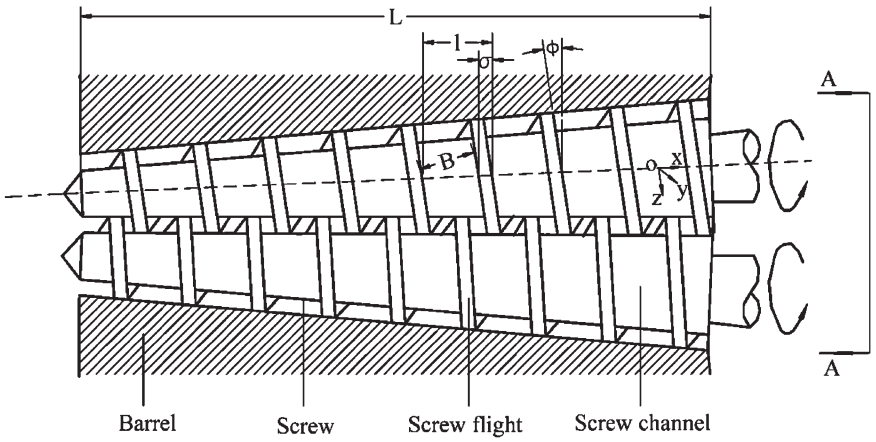

(a) Intermeshing co-rotating twin-screw elements

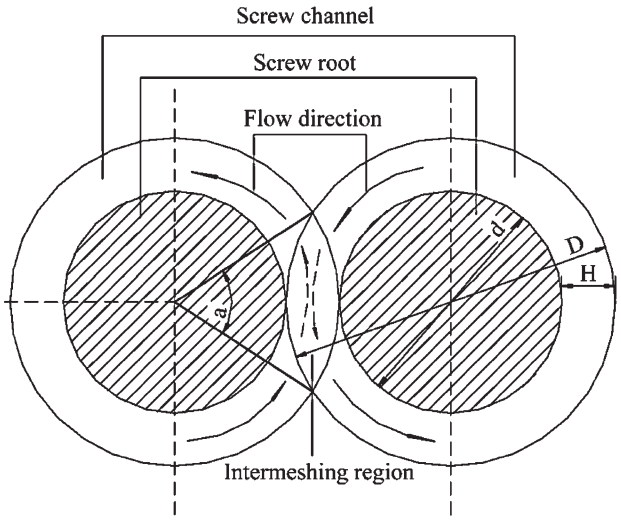

A - A

(b) A - A cross section of the extruder.

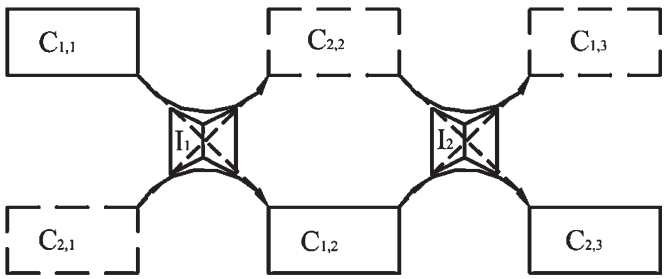

$C_{i,j}$: the jth "C" chamber of the ith screw

I_j : the jth intermeshing chamber

(c) Flow sequences in the extruder

Figure 1. Cross-sections and flow diagram of a typical intermeshing, co-rotating twin-screw extruder.

(2) The width of the channel in the intermeshing region reduced gradually to the minimum in the middle point and then increased gradually to its original value as shown in Figure 1b. The cross-section of the channel was described by an equivalent rectangle with average height H_{in} and width B_{in}.[2]

Table I. Extruder Geometry and Dimensions Used in Experiments and Model

Initial Barrel Diameter (mm)	End Barrel Diameter (mm)	Initial Screw Diameter (mm)	End Screw Diameter (mm)	Axial Width of Flight at the Tip (mm)	Axial Width of Flight at the Bottom (mm)	Pitch of Screw Channel (mm)	Axial Length of Screw (mm)
42.5	27.5	27.5	12.5	2.5	7.0	12.5	350.0

The geometric dimensions of the selected extruder are given in Table I. The total flight number, N, was determined by

$$N = \frac{L}{l} \tag{1}$$

The down channel was characterized by its height, width, and length. For the selected screw, the height of the channel, which was the flight height, was constant through the helix screw channel. The height of the "C" and intermeshing region was given by

$$\bar{H} = H_{cn} = H_{in} = \frac{D_{b1} - D_{s1}}{2} = \frac{D_{b2} - D_{s2}}{2} \tag{2}$$

The barrel and screw diameters decreased gradually along the axis of extruder to obtain a given compression ratio. The internal diameter of barrel and the diameter of screw root at the nth flight were calculated linearly by

$$D_{bn} = D_{b1} - \frac{n}{N}(D_{b1} - D_{b2}) \tag{3}$$

$$D_{sn} = D_{s1} - \frac{n}{N}(D_{s1} - D_{s2}) \tag{4}$$

The average helix angle of the screw channel at the nth flight, $\bar{\phi}_n$, was calculated by

$$\bar{\phi}_n = \tan^{-1}\left(\frac{l}{\pi \bar{D}_n}\right) \tag{5}$$

where $\bar{D}_n = (D_{bn} + D_{sn})/2$.

The overlap angle of the two screws in the intermeshing region at the nth flight, α, was calculated by

$$\alpha_n = 2\cos^{-1}\left(\frac{D_{bn} - \bar{H}}{D_{bn}}\right) \tag{6}$$

The helix length of the nth C-shaped chamber was calculated by

$$S_{cn} = \frac{(\pi - \alpha_n/2)\bar{D}_n}{\cos\bar{\phi}_n} \tag{7}$$

The helix length of the nth intermeshing chamber was calculated by

$$S_{in} = \frac{(\alpha_n/2)\bar{D}_n}{\cos\bar{\phi}_n} \tag{8}$$

The cross-section of the channel had a trapezoidal shape. The average width of the nth C-shaped chamber was calculated by

$$B_{cn} = \left(l - \frac{\sigma + \sigma'}{2}\right)\cos\bar{\phi}_n \tag{9}$$

The minimum width of the nth intermeshing chamber was calculated by

$$B_{in,\min} = [l - (\sigma + \sigma')]\cos\bar{\phi}_n \tag{10}$$

Thus, the average width of the nth intermeshing chamber was given by

$$B_{in} = \frac{B_{cn} + B_{in,\min}}{2} \tag{11}$$

Fluid Flow

There are two types of flow in the extruder: (1) plug flow of granular particles in the conveying section and (2) non-Newtonian melt flow in the other sections and die channel. The following assumptions were made for modeling the fluid flow and mixing:

(1) The flow through the intermeshing chambers was assumed to be controlled by the minimum cross-sectional area, which was given by

$$A_{in,\min} = B_{in,\min} \times H_{in} \tag{12}$$

The flow from each C-shaped chamber was divided into two streams. There were two flow streams from two C-shaped chambers entering an intermeshing chamber in the opposite directions,

the ratio of each flow entering the intermeshing chamber was determined by

$$x_f = \frac{0.5 A_{in,\min}}{A_{cn}} \tag{13}$$

The theoretical flow division ratio is between 0 and 1. The flow division ratio could be affected by the viscosity of materials and operating conditions besides extruder configuration. Sastrohartono et al.[6] found that the flow division ratio for a tangential twin-screw extruder was close to 0.5, which is close to the area ratio in our case.

(2) The flow configuration was simplified by treating the screw as stationary and rotating the barrel in the opposite direction to that of the screw.[6,11,12] The barrel thus moved at a constant relative velocity, u_b, and at the helix angle, ϕ_b, to the down channel direction.

(3) It was assumed that there was no pressure development in the conveying section since twin-screw extruders operate predominantly under starved feed conditions.[11,12]

(4) In order to simplify the transport phenomena of the non-Newtonian melt flow in the screw channel, the flow was assumed to be laminar, the gravitational forces and the inertia terms in the Navier–Stokes equation were neglected due to the high viscosity of the flow, the flow was fully developed, there was no slip at the walls, and the diffusion of momentum in the down channel z-direction was negligible.[12]

In the conveying section of the extruder, the granular particles of starch were trapped between flights of the screw and conveyed in a manner similar to the action of a screw conveyor. Friction force between the solid particle bed and barrel surface controlled the solid plug flow in the screw channel. The velocity of the plug flow in the C-shaped chambers was determined by

$$u_{cz} = \pi D_{b^n} N_s \cos \phi_{bn} \tag{13a}$$

where the helix angle of the screw channel at the nth flight tip is $\phi^{bn} = \tan^{-1}(l/\pi D_{b^n})$.

The maximum conveying capacity of the C-shaped chamber in each screw channel was calculated by

$$\dot{V}_{cz} = B_{cn} H_{cn} u_{cz} \tag{14}$$

When the material was fed into the twin-screw extruder, the material was distributed into two identical screw channels. Thus, the mass flow rate of the downstream in the C-shaped region of each screw channel was half of the mass feed rate

$$\dot{m}_{cz} = 0.5\, \dot{m}_f \tag{15}$$

Thus, the bulk density of the solid particle bed in the conveying section was determined by

$$\rho_s = \frac{\dot{m}_{cz}}{\dot{V}_{cz}} \tag{16}$$

As the selected screw had a tapered shape, the volumetric flow rate $\dot{V}_z$, which was calculated by Equation (14) decreased along the downstream channel, resulting in an increase in bulk density of the solid particles. The screw finally became completely full.

The velocity of the plug flow in the intermeshing region was assumed to be the velocity at the entrance of the intermeshing chambers since no friction between solid particles and screw surface was considered. The mass flow rate of each downstream in the intermeshing chambers was expressed as

$$\dot{m}_{tz} = x_f \dot{m}_{cz} \tag{17}$$

During extrusion, the temperature of the solid particles increases along the down channel due to the heat transfer from the hot barrel. When melting occurs, pressure is built up to push the melt along the rest of the downstream channel, forcing the melt flow through a die. In a sequence of C-shaped chambers as shown in Figure 1c, the melt flow was described as a combination of drag-pressure flow. Thus, the governing equations of momentum were written as

$$\frac{\partial P}{\partial x} = \frac{\partial}{\partial y}\left(\eta \frac{\partial u_x}{\partial y}\right) \text{in the } x\text{-direction} \tag{18}$$

$$\frac{\partial P}{\partial y} = 0 \text{ in the } y\text{-direction} \tag{19}$$

$$\frac{\partial P}{\partial z} = \frac{\partial}{\partial x}\left(\eta \frac{\partial u_z}{\partial x}\right) + \frac{\partial}{\partial y}\left(\eta \frac{\partial u_z}{\partial y}\right) \text{ in the } z\text{-direction} \tag{20}$$

The boundary conditions of the momentum equations were given by

$$u_x|_{y=0} = 0 \text{ and } u_x|_{y=H_{cn}} = \pi D_{bn} N_s \sin \phi_{bn} \tag{21}$$

$$u_z|_{x=0} = 0 \text{ and } u_z|_{x=B_{cn}} = 0 \tag{22}$$

$$u_z|_{y=0} = 0 \text{ and } u_z|_{y=H_{cn}} = \pi D_{bn} N_s \cos \phi_{bn} \tag{23}$$

Since there was no drag effect of the barrel on the flow in the intermeshing chambers, the melt was pushed through the intermeshing chambers in a manner of positive displacement. The positive displacement resulted in a decrease in pressure. The positive displacement through the intermeshing chambers was also governed by Equations (18)–(20). However, as there was no effect of barrel drag force in the intermeshing chambers, the boundary conditions became

$$u_x|_{y=0} = 0 \text{ and } u_x|_{y=H_{in}} = 0 \tag{24}$$

$$u_z|_{x=0} = 0 \text{ and } u_z|_{x=B_{in}} = 0 \tag{25}$$

$$u_z|_{y=0} = 0 \text{ and } u_z|_{y=H_{in}} = 0 \tag{26}$$

Equations (18)–(26) were used to predict the flow patterns and pressure gradients in the C-shaped chambers and the intermeshing chambers. Both the pressure gradients and velocities in Equations (18) and (26) were unknown. In order to evaluate the pressure gradients and flow patterns, continuity equations were used to solve the momentum and the continuity equations iteratively.

The integral form of the continuity equations in the C-shaped chambers was given by

$$\int_0^H \rho_m u_x \, dy = \dot{m}_{cx} \text{ in the } x\text{-direction} \tag{27}$$

$$\int_0^{B_{cn}} \int_0^H \rho_m u_z \, dx \, dy = \dot{m}_{cz} \text{ in the } z\text{-direction} \tag{28}$$

where $\dot{m}_{cx}$ was the leakage flow rate across flights which was assumed to be zero for small fight clearance and $\dot{m}_{cz}$ was the downstream channel flow rate in the C-shaped chambers given by Equation (15).

The integral form of the continuity equations in the intermeshing chambers were given by

$$\int_0^H \rho_m u_x \, dy = \dot{m}_{ix} \text{ in the } x\text{-direction} \tag{29}$$

$$\int_0^{B_{in}} \int_0^H \rho_m u_z \, dx \, dy = \dot{m}_{iz} \text{ in the } z\text{-direction} \tag{30}$$

where $\dot{m}_{tx}$ was the leakage flow rate across flights which was assumed to be zero for small flight clearance and $\dot{m}_{tz}$ was the downstream channel flow rate in the intermeshing chambers given by Equation (17).

The net pressure generation in the screw was the sum of pressure generation in each "C" chamber and pressure drop in each intermeshing chamber, which was expressed as

$$\Delta P_s = \sum_{n=1}^{N} \Delta P_{cn} - \sum_{n=1}^{N} \Delta P_{in} \tag{31}$$

where ΔP_{cn} was the pressure generation through the nth C-shaped chamber and ΔP_{in} was the pressure drop through the nth intermeshing chamber.

The extrusion die serves as a major tool for the production of products. Flow in the die was assumed to be isothermal non-Newtonian fluid. Because the cylindrical hole of the die was symmetrical with the axis, only half of the axial cross-section was chosen for analysis. The governing equation of momentum was written as

$$\frac{\partial P}{\partial z} = \frac{1}{r}\frac{\partial}{\partial r}\left(\eta r \frac{\partial u_z}{\partial r}\right) \tag{32}$$

The boundary conditions of the above equation were given by

$$\left.\frac{\partial u_z}{\partial r}\right|_{r=0} = 0 \text{ and } u_z|_{r=R} = 0 \tag{33}$$

In order to solve the momentum equation, the continuity equation was used to iteratively determine the pressure gradient in Equation (32). The continuity equation was written as

$$\int_0^R (\rho_m \times 2\pi r u_z) dr = \dot{m}_f \tag{34}$$

The melt was assumed to follow the power law, and the viscosity of the melt was calculated by[13]

$$\eta = 106.25\gamma^{-0.63} \exp\left(\frac{2451}{T_K}\right) \exp(-4.63X_w) \tag{35}$$

where the shear rate was calculated by

$$\gamma = \left[\left(\frac{\partial u_x}{\partial y}\right)^2 + \left(\frac{\partial u_z}{\partial x}\right)^2 + \left(\frac{\partial u_z}{\partial y}\right)^2\right]^{\frac{1}{2}} \quad \text{(in screw channel)} \tag{36}$$

$$\gamma = \frac{\partial u_z}{\partial r} \text{ (in die channel)} \tag{37}$$

The working point of the extruder for given processing conditions was determined by the pressure balance over the whole extruder. The net pressure generation in the screw, ΔP_s, should equal the pressure drop through the die, ΔP_d.

Heat Transfer and Melting Kinetics

During extrusion, starch particles enter the extruder, transform to a melt at some point within the extruder due to heating, and move toward the exit of the extruder. As a co-rotating intermeshing twin-screw extruder has high mixing capacity, it is normally assumed that product temperature is uniform in the direction normal to the screw shafts and heat transfers from the hot barrel to the material by convection.[7,8,14]

It has been reported that co-rotating twin-screw extrusion follows a particle dispersed melting mechanism.[9,10,15] In the particle dispersed melting model, the solid particles are assumed to be uniform, spherical, and dispersed in a melt matrix as shown in Figure 2a. Rauwendaal[9] reported that a minimum volume of polymer melt has to be available to fill the space between the solid particles before the solid particle flow becomes a non-Newtonian melt flow. Wang et al.[16] found that the powdery raw starch became interconnected and behaved like a fluid when the percent conversion of starch reached about 37%.

Therefore, the following assumptions were made for modeling the melting kinetics and heat transfer:

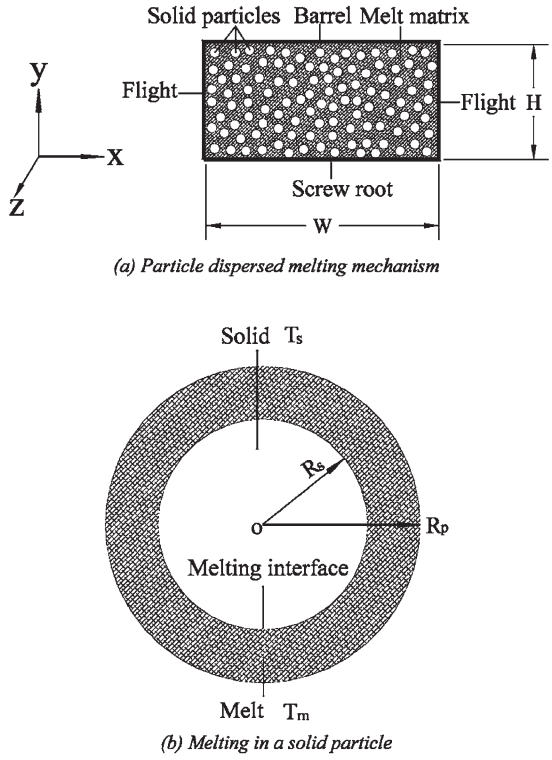

Figure 2. Particle dispersed melting mechanism in a twin-screw extruder.

(1) The solid particles which were fed into the extruder were assumed to be identical. Therefore, one particle was chosen for the analysis of melting kinetics.
(2) Initially, the particle was heated from initial feed temperature to the melting temperature at 115°C [8] by the hot barrel. The energy due to internal friction between starch particles was neglected. The melting of the particle occurred when its surface temperature reached the melting point.
(3) When the percent conversion of starch particles to melted starch reached about 37%,[16] the particle plug flow became non-Newtonian melt flow. The heat transfer from the hot barrel and the heat of viscous dissipation in the melt matrix continued to melt the particle and increased the melt temperature.
(4) The convective heat from the hot barrel and the heat of viscous dissipation in the melt were uniformly distributed to each particle.

During melting, there existed a moving interface within the particle, which moved from the surface to the center of the particle until the whole particle was melted. The moving interface divided the whole particle into two regions: the core solid region and the outer melt layer as shown in Figure 2b. The heat transfer through the solid core region was governed by

$$\rho_s c_s \frac{dT_s}{dt} = \frac{1}{r^2}\frac{\partial}{\partial r}\left(r^2 k_s \frac{\partial T_s}{\partial r}\right) \tag{38}$$

The heat transfer through the outer melt layer was governed by

$$\rho_m c_m \frac{dT_m}{dt} = \frac{1}{r^2}\frac{\partial}{\partial r}\left(r^2 k_m \frac{\partial T_m}{\partial r}\right) + \dot{q}_m \tag{39}$$

where the viscous heat generation rate in the melt, $\dot{q}_m$, was given by

$$\dot{q}_m = \eta\gamma^2 \tag{40}$$

Boundary conditions were

$$\left.\frac{\partial T_s}{\partial r}\right|_{r=0} = 0 \tag{41}$$

$$T_s|_{r=R_s} = T_m|_{r=R_s} = T_{m0} \tag{42}$$

$$k\left.\frac{\partial T}{\partial r}\right|_{r=R_p} = q_{\text{sur}} \tag{43}$$

where q_s is the heat flux on the surface of the particle.

The location of the moving interface, r_s, was determined by the energy balance on the interface. On the interface, the net heat conduction was equal to the latent heat of melting, which was expressed as

$$k_s\left(\frac{\partial T_s}{\partial r}\right) - k_m\left(\frac{\partial T_m}{\partial r}\right) = \lambda\rho_s\frac{\mathrm{d}r_s}{\mathrm{d}t} \tag{44}$$

It should be noted that before melting occurred, heat transfer through the particle was governed only by Equation (38) with boundary conditions given by Equations (41) and (43). The melt fraction was expressed as the ratio of melt volume to the total volume of the particle, which was given by

$$\theta_m = \frac{v_m}{v_p} \tag{45}$$

When the flow advanced for a Δz step in the downstream direction, the total particles enclosed by the small volume of $\Delta z \times B \times H$ were determined by

$$N_p = \frac{\dot{m}_z\Delta t}{\rho_p v_p} \tag{46}$$

where Δt is the residence time for the Δz distance.

When particles entered the intermeshing chambers, there was no convection heat transfer between the particles and the hot barrel wall. However, in the C-shaped chambers, convection heat transfer occurred. When particles advanced for a Δz_c step in the downstream direction of the C-shaped chambers, the total heat transfer between the particles and the hot barrel was calculated by

$$Q_b = h\,B_{cn}\Delta z_c(T_{b,\mathrm{sur}} - T_{p,\mathrm{sur}}) \tag{47}$$

For the particle bed, a pseudo-heat transfer coefficient, h, was expressed as the dependence on the density of the particle bed

$$h = a\rho^b \tag{48}$$

In order to determine constants a and b in the above equation, two sets of h and ρ were required. It was assumed that for the channel filled with air only, h = 30 W/(m^{2}K) and ρ = 1 kg/m^3 and for the channel fully loaded with particles, h = 1500 W/(m^{2}K) and ρ = 416 kg/m^3. In this case, a = 30 and b = 0.65.

The total heat, Q_b, was uniformly distributed to each particle in the small analyzed volume, and the heat flux on the particle surface, q_{sur} in Equation (43) was thus given by

$$q_{\mathrm{sur}} = \frac{Q_b}{N_p A_{p,\mathrm{sur}}} \tag{49}$$

The temperature of the bulk flow was the mass average temperature of the particle, which was given by

$$T_{\mathrm{aver}} = \frac{\int_{V_p} T(r)\mathrm{d}m}{\int_{V_p}\mathrm{d}m} = \frac{\sum_{i=1}^{E}\frac{2}{3}\pi\left(T_{i2}r_{i2}^3 - T_{i1}r_{i1}^3\right)}{\sum_{i=1}^{E}\frac{4}{3}\pi\left(r_{i2}^3 - r_{i1}^3\right)} \tag{50}$$

Mixing

As mentioned above, the flow from a C-shaped chamber was divided into two streams at the entrance of an intermeshing chamber and two streams were merged at the exit of the intermeshing chamber. For each repeated turn, all particles had 100% possibility flowing through a C-shaped chamber and x_f × 100% possibility of flowing through an intermeshing chamber. Therefore, at the exit of each intermeshing and C-shaped chamber, the velocity, temperature, and melt fraction were adjusted by

$$u = u_{cn} + x_f u_{in} \tag{51}$$

$$T = T_{cn} + x_f T_{in} \tag{52}$$

$$\theta = \theta_{cn} + x_f\theta_{in} \tag{53}$$

Simulation Approach

A computer program was written to solve the model. The program was divided into four parts to obtain solutions for geometrical parameters, fluid flow, heat transfer, and melting kinetics. The simulation began with the input of geometries of the extruder, processing conditions, and relevant constants. The total flight turns were determined by Equation (1). The height, helix length and width of each C-shaped chamber and intermeshing chamber were determined by Equations (2)–(11). The leakage flow ratio of a stream entering the intermeshing chamber was determined by Equation (13).

The helix length, height, and width of the "C" chamber and intermeshing chamber were then divided into ten sections along the downstream channel, respectively. The radius of a particle was divided into ten segments. Simulations were advanced from the first cross-section at the entrance of the C-

shaped chamber to the last cross-section at the exit, and the entrance of the intermeshing chamber to the last cross-section at the exit. In the program, a finite element scheme was used to solve partial differential Equations (18), (20), (32), (38), and (39).

For the solid particle flow in the conveying section, the velocity and volumetric flow rate of the downstream were calculated by Equations (13) and (14). The bulk density of the solid particle bed was then determined by Equation (16). The temperature distribution in the particle was predicted by Equations (38), (41), and (43). The temperature of the bulk flow was then determined by Equation (50). The surface temperature of the particle was then compared with the melting temperature. If the surface temperature of the particle was smaller than the melting temperature, there was no melting and the analysis of plug flow continued on to the next cross-section. Otherwise, melting occurred and the melting rate was determined by Equation (44). If the volumetric melt fraction was less than 37% of the total particle volume, the analysis of plug flow continued on the next cross-section. The temperature distribution in the particle was predicted by Equations (38)–(43). Otherwise, the material became a melt flow. The velocity and pressure profiles in the melt were obtained by Equations (18)–(30). The melting rate was determined by Equation (44). The temperature distribution in a particle was predicted by Equations (38)–(43). The analysis proceeded until the last cross-section, at the exit of the "C" chamber or the intermeshing chamber, was reached. At the exit of each C-shaped and intermeshing chamber, the velocity, temperature, and melt fraction were adjusted by Equations (51)–(53). The analysis advanced to the next C-shaped chamber and intermeshing chamber until the exit of the screw channel was reached.

Finally, the non-Newtonian fluid entered into the die channel. As indicated in Figure 3, there were four sections in the die. The radius of each section was divided into 50 segments, and the length of each section was divided into 100 segments each. The velocity and pressure of each node formed the velocity and pressure fields in the die channel. The pressure gradient and velocity profile in the die channel were predicted by Equations (32)–(34). The simulation was stopped when the last cross-section at the exit of the die channel was reached.

Materials and Methods

Normal corn starch (~25% amylose and ~75% amylopectin) purchased from National Starch and Chemical Co. (Bridgeport, NJ) was used in the experiments. The moisture content of the starch was adjusted to the different levels by blending with distilled water. The samples were sealed in plastic buckets and stored at 4°C for one day. Before extrusion, the samples were removed from cold storage and allowed to come to room temperature. The moisture contents of samples were measured by a moisture analyzer at the chamber temperature of 105°C (HG 53 moisture analyzer, Mettler-Toledo GmbH, Laboratory & Weighing Technologies, Greifensee, Switzerland). The properties of granular and melted starch are given in Table II.

The starch was extruded in a twin-screw laboratory extruder (model CTSE-V, C. W. Brabender, Inc., South Hackensack, NJ). Two conical screws co-rotated inside the barrel of the extruder. The conical screws had diameters decreasing from 42.5 to 27.5 mm along an axial length of 350 mm from the feed end to the exit end. The detailed dimensions of the extruder are given in Table I. Three die nozzles with different diameters were used. The dimensions of three die nozzles and operating conditions are given in Table III.

Starch was fed into the extruder using a FlexWall® Plus Feeder (Brabender Technologie, Inc., Ont., Can-

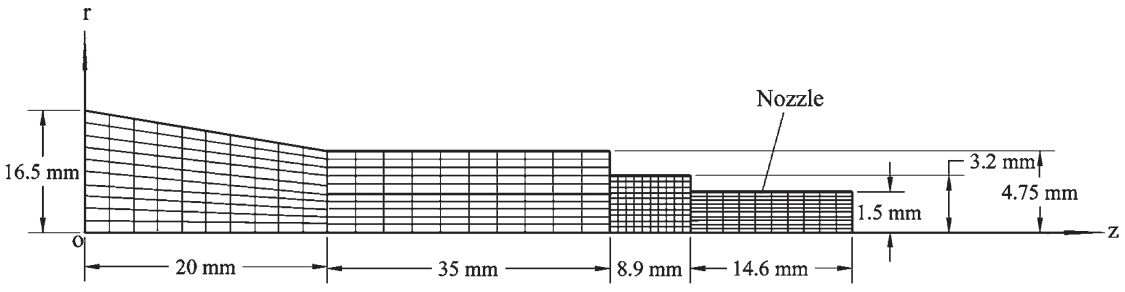

Figure 3. Geometry of die and finite element arrangement in the die channel.

Table II. Properties of Granular and Melted Starch Used in Model

Specific heat (J/(kg K))	$c = 1291 + 2321 X_w$ [18]	$c = 1291 + 2321 X_w$ [18]
Density (kg/m^3)	$\rho_s = \frac{\dot{m}_z}{\dot{V}_z}$ ($P = 0$ Pa)	$\rho_m = 1200$ [13]
Thermal conductivity (W/(m K))	$k_s = (1 - \varepsilon_v)k_p + \varepsilon_g k_g$ [19], where	$\frac{1}{k_m} = \frac{(1-\varepsilon_w)}{k_{ds}} + \frac{\varepsilon_w}{k_w}$ [20], where
	$\varepsilon_g = 1 - \frac{\rho_s}{\rho_p}$	$\varepsilon_w = \frac{\rho_{ds} X_w}{\rho_w + \rho_{ds} X_w}$
	$k_p = (1 - \varepsilon_w)k_{ds} + \varepsilon_w k_w$	
	$k_{ds} = 0.0976 + 0.167 \times 10^{-2} T$	$k_{ds} = 0.21 + 0.41 \times 10^{-3}(T + 273.15)$
	$k_w = 0.571 + 1.76 \times 10^{-3} T - 6.70 \times 10^{-6} T^2$	$k_w = 0.571 + 1.76 \times 10^{-3} T - 6.70 \times 10^{-6} T^2$
	$k_g = 0.00324 + 5.31 \times 10^{-4} T$	
Melting latent heat (J/g)	–	$\lambda = 13.8$ [21]

Table III. Experimental and Predicted Process Variables and System Variables

Die Nozzle		Process Variable						Experimental Data			Predicted Data				
D_n (mm)	L_n (mm)	N (rpm)	$\dot{m}_f$ (kg/h)	M_w (%)	T_{b1} (°C)	T_{b2} (°C)	T_{b3} (°C)	T_{dw} (°C)	P_d (MPa)	T_d (°C)	t_{min} (s)	$P_d{}^a$ (MPa)	$P_d{}^b$ (MPa)	T_d (°C)	t_{min} (s)
3.0	14.6	140	7.73	16	67	134	139	113	11.13	142	22	10.49	10.41	148.8	30.6
3.0	14.6	140	8.86	24	72	141	140	125	6.78	139	24	6.65	6.24	141.8	26.6
3.0	14.6	160	7.34	20	64	136	139	124	8.56	140	20	7.90	7.11	144.9	25.5
4.0	14.6	140	8.86	24	67	130	139	127	4.48	139	22	3.81	4.03	133.5	19.3
4.0	14.6	120	6.11	20	65	125	130	107	6.27	139	30	6.48	5.84	136.0	29.8
5.0	14.7	140	7.73	16	69	129	132	104	7.78	137	19	7.21	6.32	137.5	23.1
5.0	14.7	140	8.86	20	65	134	137	112	5.36	142	20	5.66	4.82	138.0	21.9

[a] Die pressure based on pressure rise through the screw channel.
[b] Die pressure based on pressure drop through the die channel.

ada), maintaining as constant a feed rate as possible. The extruder was controlled by a plasti-Corder (type FE 2000, C. W. Brabender, Inc., NJ). The barrel temperatures and the product temperature at the die entrance were recorded using temperature probes (Omega Engineering Inc., CT). The operating pressure at the die entrance was recorded using a pressure transducer (model PT 411-10M-6, Dynisco Inc., MA). The exact rotational speeds, barrel temperatures, and die pressure were recorded automatically during extrusion.

A stimulus response technique was used to measure the minimum residence time. The stimulus was a color dye tracer. During extrusion, the tracer was added to the feeding zone and the minimum time for the tracer to go through the extruder was recorded. In simulation, the minimum residence time was the shortest distance divided by the maximum velocity of downstream flow. The shortest distance is the total helix length of the C-shaped chambers on a screw. The maximum velocity of downstream flow was obtained by the velocity distribution profile. All extrusion runs were conducted in triplicate.

Results and Discussion

Model Validation

In order to validate the model, predictions of the model were compared with the measured values for seven arbitrarily selected experimental conditions. The operating conditions and predicted and measured results are given in Table III. Standard errors between the predicted and experimental product pressure and bulk temperature at the die entrance, and minimum residence time were about 8.8, 2.8, and 17.3%. On one hand, the accuracy of the measure-

ments was a likely reason for the variations between the predicted and experimental data. On the other hand, for improving the accuracy of the model, more research is needed particularly on the densities of the solid bed and melt, the rheological properties of the melt, the latent heat of melting, and the moisture loss of the starch during extrusion.

Profiles of Bulk Temperature and Pressure

Typical profiles of bulk temperature and pressure along the extruder during extrusion are given in Figure 4. The curve of the bulk temperature profile shows there are three different increasing rates of bulk temperature along the extruder (Figure 4). When entering into the feed zone at an initial temperature of 25°C, the material was heated to only 50°C at the end of the first heating zone due to the poor thermal conductivity of the starch particle bed and the low barrel temperature. The material then entered into the second heating zone with a higher barrel temperature. The heating rate of starch increased in the second heating zone due to a higher barrel temperature. When melting occurred and the particle flow became a melt flow in the second heating zone, there was a sharp increase in bulk temperature due to the heat of viscous dissipation and higher thermal conductivity of the melt. However, at the end of extrusion, the heating rate of starch slowed down due to the decrease in temperature difference between the barrel surface and the melt, and a decrease in the heat of viscous dissipation at high bulk temperature.

In the conveying section of the extruder where relatively free-flowing granular particles exist, internal shear of the material was negligible and the pressure was zero as shown in Figure 4. The loose particle starch was initially conveyed toward the direction of the die by the rotating screw. Along the extruder, the particles were heated by the barrel. When the surface temperature of the particles reached their melting temperature, melting occurred. The particles were compressed along the extruder due to the decrease of cross-sectional area in the tapered screw channel and the cohesive effect of melted particle surface. When the melt to particle fraction approached 37% by volume, the starch material became a non-Newtonian melt fluid and pressure developed in the starch melt as shown in Figure 4. It can be seen from Figure 4 that the pressure rise in the screw channel equaled the pressure drop in the die channel. The positive pressure difference between the entrance and the exit of the die forced the melt through the die channel by overcoming the flow resistance in the die nozzle. It should be noted that only when the extruder operates

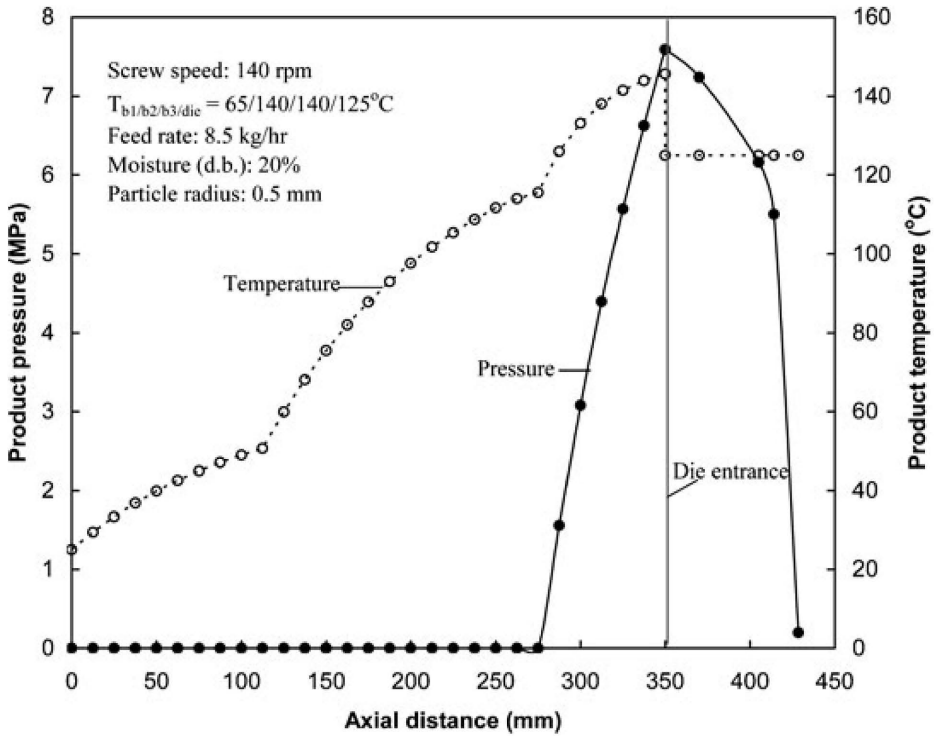

Figure 4. Predicted pressure and temperature profiles within the extruder.

at its operating point, a good match between pressure rise in the screw channel and the pressure drop in the die channel can be achieved. Each extruder has its operating characteristics.[17] Before operating an extruder, it is essential to know its characteristic curves for setting the operating conditions. For a given extruder, the characteristic curves can be generated by simulation or experiments.[17]

Figure 5 shows typical pressures in a C-shaped chamber and the pressure drop in an intermeshing chamber. The predicted pressure in one C-shaped chamber was 1–2 MPa, and the pressure drop in an intermeshing chamber was 0.25–0.35 MPa. The data are close to those for similar conditions reported by Tayeb et al.[3] In the intermeshing chamber, there was no drag effect on the flow from the barrel wall. The material was pushed through the gap between the two screws by the pressure difference at the entrance and exit of the chamber. As a result, the pressure decreased gradually from the entrance to the exit of the intermeshing chamber. In the C-shaped chamber, drag flow, and pressure flow existed in the non- Newtonian melt. Drag flow was the flow toward the discharge end of the screw resulting from viscous drag. Pressure flow was dependent on the pressure gradient in the screw channel. As shown in Figure 6, the velocities near the barrel wall were positive as drag flow along the barrel wall was directed toward the die of the extruder. The velocities near the screw surface were negative in the direction of pressure flow toward the feeder of the extruder. Both drag and pressure flows maintained the prescribed downstream mass flow rate.

The drag flow decreased in the C-shaped chambers along the extruder due to the decrease in cross-sectional area and the decrease in apparent viscosity of the dough with increase in melt temperature. With a decrease in drag flow, the pressure flow simultaneously decreased to maintain a given downstream mass flow rate in the C-shaped chambers. Therefore, the pressure generated in the C-shaped chambers along the extruder gradually decreased as shown in Figure 5. In the intermeshing chambers, the decrease of cross-sectional area increased the pressure drop for a given downstream mass flow rate through the chambers. However, the decrease in apparent viscosity of the dough decreased the pressure drop. Both adverse effects controlled the pressure drop in the intermeshing chambers.

Melt Kinetics

The profiles of melt fraction for particles with different sizes are given in Figure 7. Profiles of starch melting along the extruder are important for the quality of final products as inefficient melting will deteriorate the

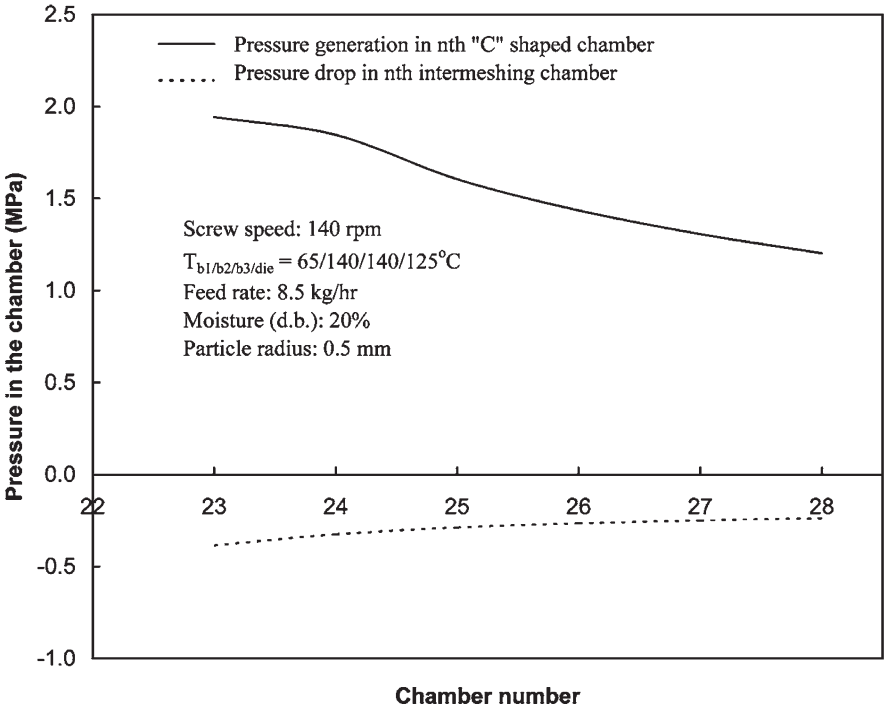

Figure 5. Pressure generation in a C-shaped chamber and pressure drop in an intermeshing chamber.

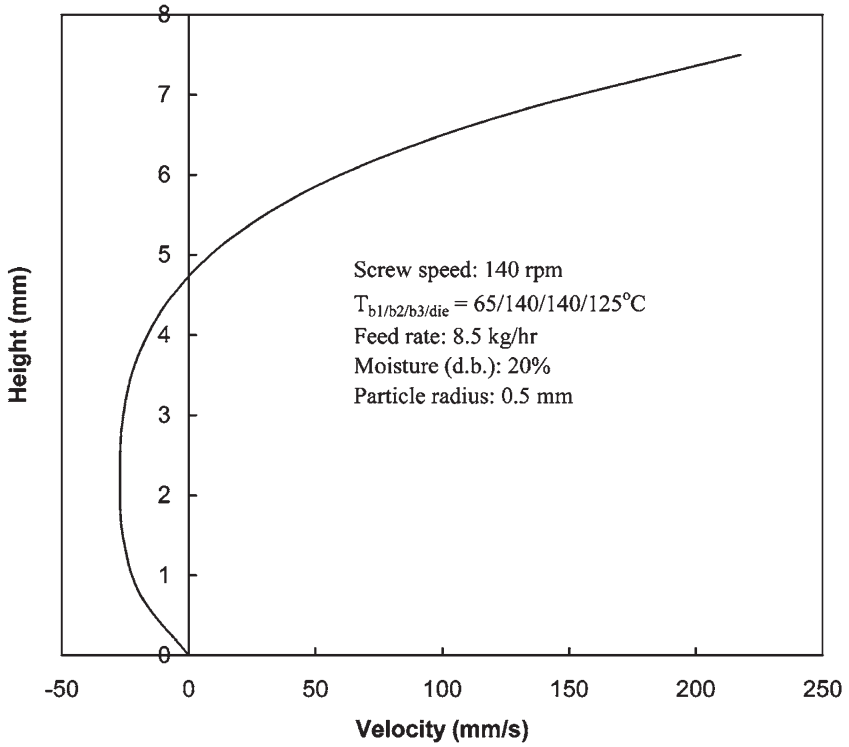

Figure 6. A typical velocity distribution of a combined drag and pressure flow along the flight height in down channel direction of a C-shaped chamber.

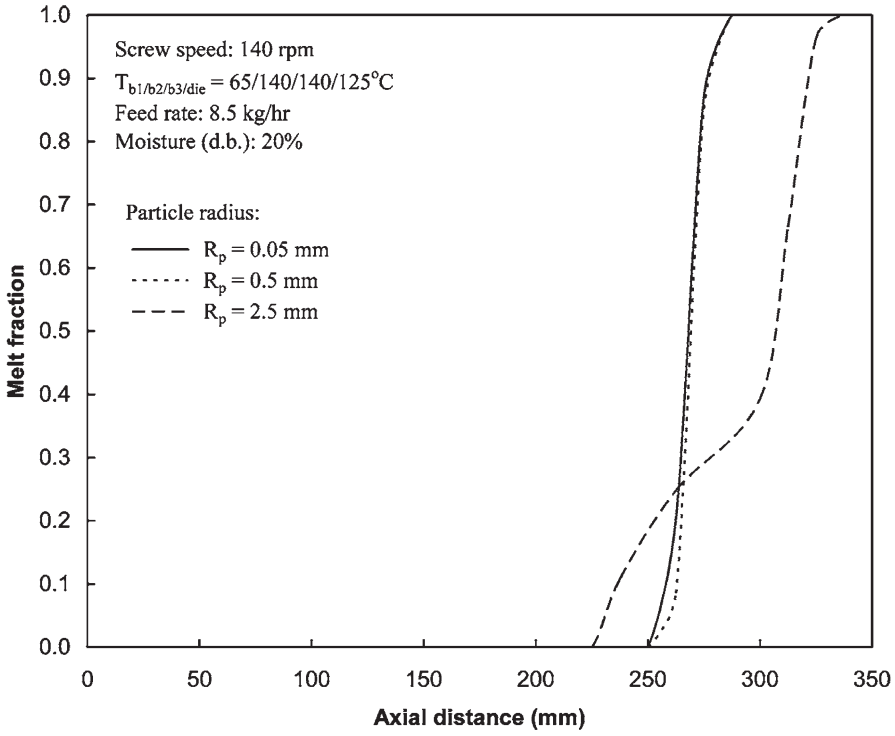

Figure 7. Predicted melt fraction along the axis of extruder.

quality of the final products. It can be seen from Figure 7 that melting of a small particle (e.g., particle radius 0.5 mm or less) was almost instantaneous. However, it took a long axial distance in the extruder to melt a large particle (e.g., particle radius 2.5 mm).

On the melt fraction curve of the large particle in Figure 7, the melting rate at the beginning was much smaller than that at the final stage. Melting is an endothermic process. At the beginning of melting, the material was still in a particle form and heat transfer from the hot barrel contributed to the latent heat of melting. When the melt to particle fraction reached a critical value (37% for starch given by Wang et al.[16]), the space between particles became filled by melt and the particle flow becomes a non-Newtonian melt flow. The heat transfer from the hot barrel and the heat of viscous dissipation in the melt matrix continued to melt the remaining part of particles, increasing the melting rate.

It also can be seen from Figure 7 under the same operating conditions, the melting of a large particle started earlier than that of a small particle. To further explain this phenomenon, predicted temperature distributions in a large particle and in a small particle are given in Figs. 8 and 9. It can be seen from Figure 8 that there was a large temperature gradient in the radial direction of the large particle during extrusion. For the particle with a radius of 2.5 mm, when the surface temperature increased to the melting point of 115°C, the central temperature of the particle was only about 30°C. The large temperature gradient in the particle existed until the particle was entirely melted. After the entire particle was melted, the temperature gradient in the melt became very small because the melt was heated mainly by the inner heat of viscous dissipation in the melt rather than heat transfer from the hot barrel. It also can be seen from Figure 8 that there was a melting interface in the particle when the surface temperature of the particle reached the melting point. The whole particle was divided into two regions by the interface: the shell melt region and the core solid region. The melting interface moved from the surface to the center of the particle and finally disappeared when the entire particle was melted. However, there was no obvious temperature gradient in a small particle as shown in Figure 9. The difference between the surface temperature and the central temperature in a small particle with a radius of 0.5 mm was less than 2°C during the whole extrusion.

The temperature distributions in Figs. 8 and 9 show that heat transfer during heating and melting of a small solid particle is mainly controlled by the con-

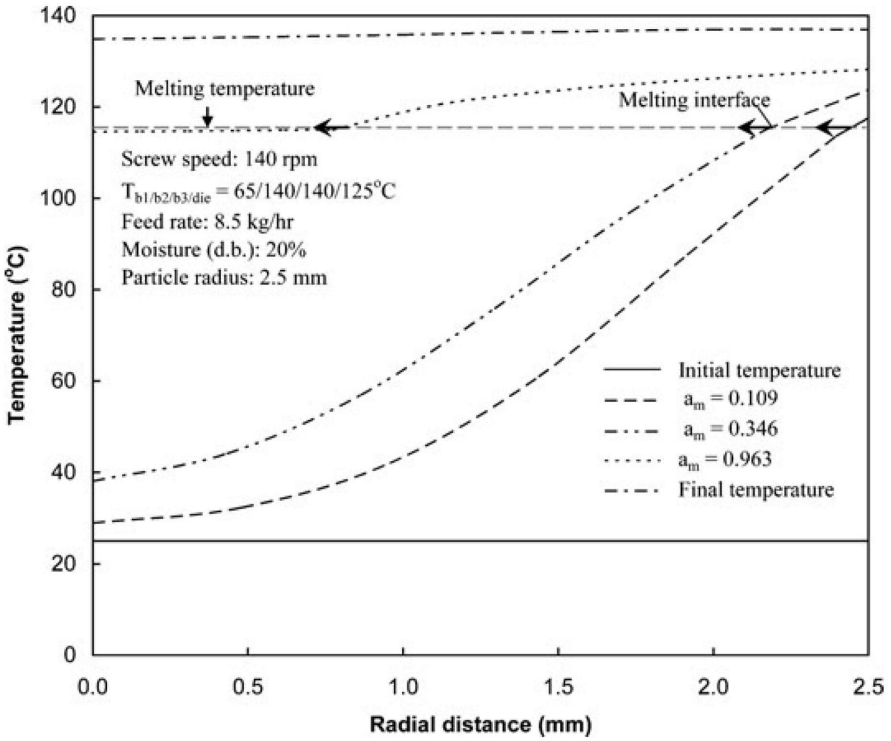

Figure 8. Temperature distribution in a large particle (radius 2.5 mm) during extrusion.

vection between the barrel surface and the material bed. However, heat transfer during heating and melting of a large particle is controlled both by convection and by conduction within the particle. This explains why the melting of a small particle was instantaneous and the melting time of a large particle was very long as shown in Figure 7.

Under the same operating conditions, the surface temperature of a larger solid particle increased faster than that of a small particle as shown in Figure 10. In the conveying zone, the temperature of powders increases due to the heat transfer between powders and the hot inner surface of the extruder barrel. The heat first transfers from the hot barrel surface to the powder surface by convection and then from the powder surface to its inside by conduction. Compared to a small powder, a large powder receives more heat from the hot barrel surface due to its larger surface area but transfers heat slowly into the inside due to its larger dimension. So, the surface temperature for the large powder is higher than that of small powders. As a result, the surface temperature of the large particle reached the melt point earlier than that of the small particle as shown in Figure 7. However, the melting rate of the large particle was smaller than that of the small particle. The small particle flow became melt flow earlier than the large particle flow as shown in Figure 7. The melt flow is accompanied by the heat of viscous dissipation. Therefore, at the end of extrusion, the surface temperature of the small particle was higher than that of large particle due to the heat of viscous dissipation as shown in Figure 10.

Effects of Particle Size on the Profiles of Bulk Temperature and Pressure

Particles with different sizes have different melting kinetics, causing different product bulk temperature and pressure profiles in the extruder. As shown in Figure 11, the bulk temperature of small particles was higher than that of large particles at the same location along the extruder under the same operating conditions. Before the particle flow became a melt flow, the particle bed was heated by convection. The convective heat transfer was a function of convection heat transfer coefficient, barrel surface area, and the temperature difference between the barrel wall and the particle surface. Under the same operating conditions, the convection heat transfer coefficient, barrel surface area, and barrel wall temperature were the same. However, as shown in Figure 10, the surface temper-

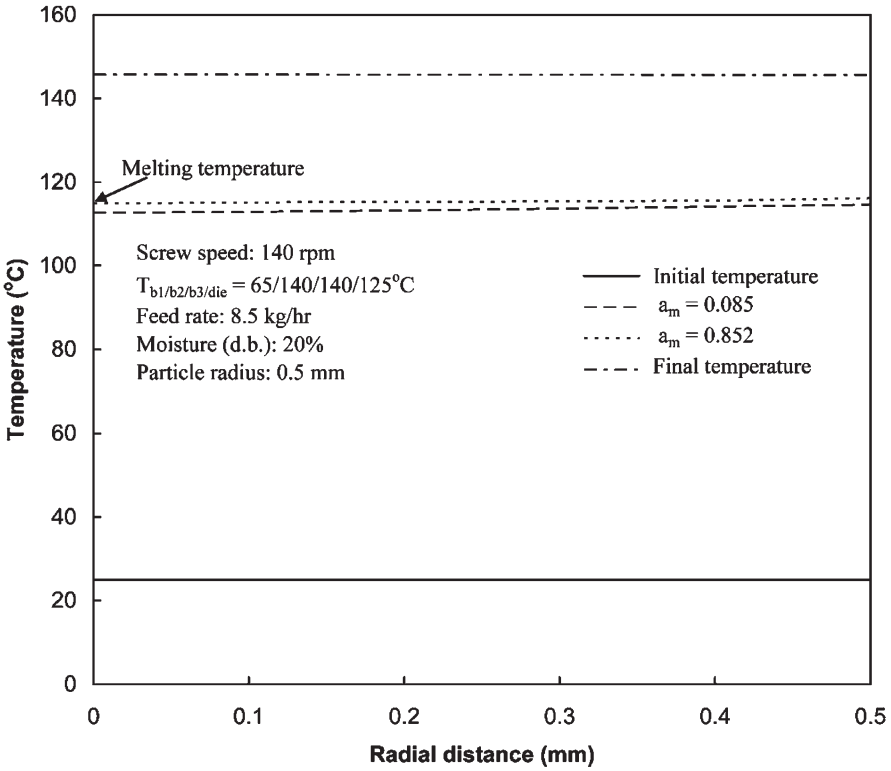

Figure 9. Temperature distribution in a small particle (radius 0.5 mm) during extrusion.

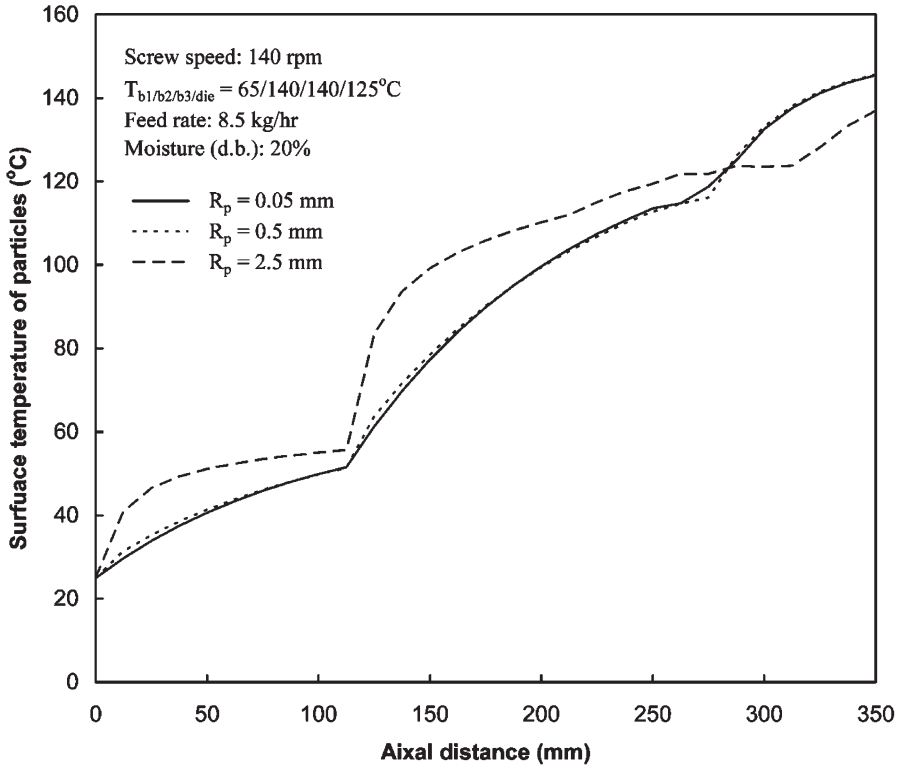

Figure 10. Predicted surface temperature profiles of particles with different sizes during extrusion.

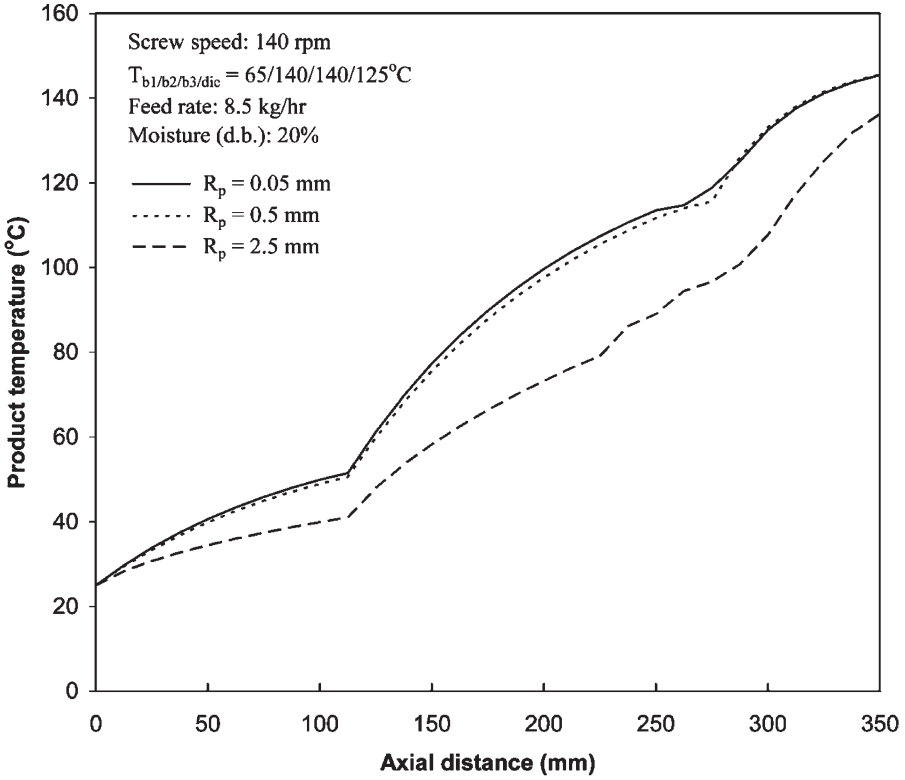

Figure 11. Predicted bulk temperature profiles in the extruder for particles with different sizes.

ature of small particles was lower than that of large particles during heating. Therefore, the small particles received more heat from the barrel wall by convection than the large particles due to larger temperature differences, resulting in higher bulk temperature along the extruder. Figure 12 shows that the product pressure of small particles was higher than that of large particles along the extruder. Pressure was developed in the melt through the remainder of the extruder after the particle flow became the melt flow. The melting of small particles was completed much faster than the melting of the large particles.

Conclusions

A mathematical model was developed to describe the co-rotating twin-screw extrusion process of biomaterials. The standard errors between the predicted and experimental product pressure and bulk temperature at the die entrance, and minimum residence time were 8.8, 2.8, and 17.3%. The melting of small particles (e.g., particle radius 0.5 mm or less) was almost instantaneous, while it took a long axial distance in the extruder to melt large particles (e.g., particle radius 2.5 mm). Different melting characteristics, product pressure, and bulk temperature profiles in the extruder were observed for different particle sizes using the model. Adjustment of operating conditions is needed for the extrusion of starch-based materials with different particle sizes for uniform product quality.

Acknowledgments

This study was conducted at the Industrial Agricultural Products Center, University of Nebraska–Lincoln, Lincoln, NE. Authors would like to recognize Dr. Girish M. Ganjyal and Mr. Robert Weber for their assistance in the experiments.

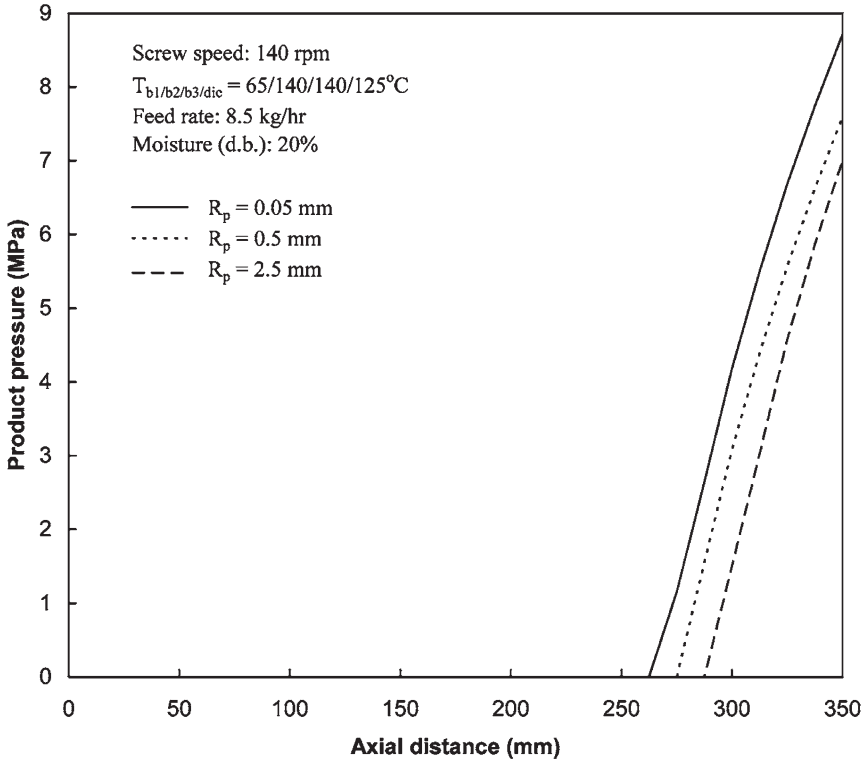

Figure 12. Predicted pressure profiles in the extruder for particles with different sizes.

Nomenclature

A	Area (m^2)
B	Channel width (m)
c	Specific heat capacity (J/(kg K))
D	Diameter (m)
$\bar{D}$	Average diameter of internal diameter of barrel and diameters of screw boot (m)
E	Total element number
H	Channel height (m)
h	Convection heat transfer coefficient ($W/(m^2 K)$)
i	The ith element
k	Thermal conductivity (W/(m K))
L	Axial length of the screw (m)
l	Pitch of screw channel (m)
m	Mass (g)
$\dot{m}$	Mass flow rate (g/s)
N	Total flight number
N_P	Total particle number
Ns	Screw speed (rpm)
P	Pressure (Pa)
ΔP	Pressure difference (Pa)
$\dot{q}_m$	Viscous heat generation rate (W/m^3)
Q	Heat transfer rate (W)
q_{sur}	Heat flux on the surface (W/m2)
R	Radius (m)
S	Channel helix length (m)
T	Temperature (°C)
T_K	Temperature on the Kelvin scale (K)
t	Time (s)
Δt	Time step (s)
u	Velocity (m/s)
v	Volume (m^3)
$\dot{V}$	Volumetric flow rate (m^3/s)
x	The mass ratio of two flow streams
X_w	Moisture (%, db)
Δz	Spatial step (mm)

Subscripts

0	Initial
1	Entrance or node 1
2	Exit or node 2
a	Constant in Equation (48)
aver	Average
b	Barrel or constant in Equation (48)
cn	The nth C-shaped chamber
cx	The width direction in the C-shaped chamber
cz	The downstream direction in the C-shaped chamber
ds	Dried solid
f	Feed
g	Gas
in	The nth intermeshing chamber
ix	The width direction in the intermeshing chamber
iz	The downstream direction in the intermeshing chamber
m	Melt
min	Minimum
n	The nth flight
p	Particle
r	r-Coordinate in the radial direction
s	Screw or solid
sur	Surface
w	Water
x	x-coordinate in the cross-width direction
y	y-coordinate in the height direction
z	z-coordinate in the down stream direction

Greek Letters

$\bar{\phi}$	Flight angle (°)
α	Overlap angle of two screws (°)
σ'	Axial width of flights at the tip (m)
σ	Axial width of flights at the bottom (m)
ρ	Density (kg/m^3)
η	Apparent viscosity (Pa s)
γ	Shear rate (1/s)
λ	Melting latent heat (J/g)
θ	Melting fraction
ε	Volumetric fraction

References

1. Yacu, W. A. *J Food Eng* 1985, 8, 1–21.
2. Tayeb, J.; Vergnes, B.; Della Valle, G. *J Food Sci* 1988a, 53, 616–625.
3. Tayeb, J.; Vergnes, B.; Della Valle, G. *J Food Sci* 1988b, 53, 1047–1056.
4. Harper, J. M. In *Biotechnology and Food Process Engineering*; Schwartzberg, H. G.; Rao, M. A. (Eds.); Marcel Dekker: New York, 1990; pp. 295–308.
5. Barres, C.; Vergnes, B.; Tayeb, J.; Della Valle, G. *Cereal Chem* 1990, 67, 427–433.
6. Sastrohartona, T.; Jaluria,Y.; Karwe, M. V. *Polym Eng Sci* 1995, 35, 1213–1221.
7. Mohamed, I. O.; Ofoli, R. Y. *J Food Eng* 1990, 12, 145–164.
8. Barres, C.; Vergnes, B.; Tayeb, J. *J Food Eng* 1991, 15, 167–185.
9. Rauwendaal, C. *Adv Polym Technol* 1996, 15, 135–144.
10. Zhu, L.; Narh, K. A.; Geng, X. *J Polym Sci, Part B: Polym Phys* 2001, 39, 2461–2468.
11. de Graaf, R. A.; Woldringh, D. J.; Janssen, L. P. B. M. *Adv Polym Technol* 1999, 18, 295–302.
12. Wang, L. J.; Ganjyal, G. M.; Jones, D. D.; Weller, C. L.; Hanna, M. A. *J Food Sci* 2004, 69, 212–223.
13. Padmanabhan, M.; Bhattacharya, M. *J Food Eng* 1993, 18, 335–349.
14. van Zuilichem, D.; van der Laan, E.; Kuiper, E. *J Food Eng* 1990, 11, 187–207.
15. Gogos, C. C.; Tadmor, Z.; Kim, M. H. *Adv Polym Technol* 1998, 17, 285–305.
16. Wang, S. S.; Qu, D.; Chiew, Y. *Starch* 1994, 46, 337–341.
17. Wang, L. J.; Ganjyal, G. M.; Jones, D. D.; Weller, C. L.; Hanna, M. A. *J Food Sci* 2004, 69, 212–223.
18. Rahman, S. *Food Properties Handbook*; CRC Press: Boca Raton, FL, 1995.
19. Maroulis, Z. B.; Shah, K. K.; Saravacos, G. D. *J Food Sci* 1991, 56, 773–776.
20. Maroulis, S. N.; Saravacos, G. D. *J Food Sci* 1990, 55, 1367–1372.
21. Lai, L. S.; Kokini, J. L. *Biotechnol Progress* 1991, 7, 251–266.